

# Volcanic cloud detection using Sentinel-3 satellite data by means of neural networks: the Raikoke 2019 eruption test case

Ilaria Petracca<sup>1</sup>, Davide De Santis<sup>1</sup>, Matteo Picchiani<sup>2,3</sup>, Stefano Corradini<sup>4</sup>, Lorenzo Guerrieri<sup>4</sup>, Fred Prata<sup>5</sup>, Luca Merucci<sup>4</sup>, Dario Stelitano<sup>4</sup>, Fabio Del Frate<sup>1</sup>, Giorgia Salvucci<sup>1</sup> and Giovanni Schiavon<sup>1</sup>

<sup>1</sup> Department of Civil Engineering and Computer Science Engineering, Tor Vergata University of Rome, 00133, Italy

<sup>2</sup> GEO-K s.r.l., Rome, Italy

<sup>3</sup> GMATICS s.r.l., Rome, Italy

<sup>4</sup> Istituto Nazionale di Geofisica e Vulcanologia, ONT, 00143 Rome, Italy

<sup>5</sup> AIRES Pty Ltd., Australia

*Correspondence to:* Ilaria Petracca ([ilaria.petracca@uniroma2.it](mailto:ilaria.petracca@uniroma2.it))

## Abstract

The accurate automatic volcanic cloud detection by means of satellite data is a challenging task and of great concern for both scientific community and aviation stakeholder due to the well-known issues generated by strong eruption events in relation to aviation safety and health impacts. In this context, machine learning techniques applied to satellite data acquired from recent spaceborne sensors have shown promising results in the last years.

This work focuses on the application of a neural network based model to Sentinel-3 SLSTR (Sea and Land Surface Temperature Radiometer) daytime products in order to detect volcanic ash plumes generated by the 2019 Raikoke eruption. A classification of meteorological clouds and of other surfaces comprising the scene is also carried out. The neural network has been trained with MODIS (MODerate resolution Imaging Spectroradiometer) daytime imagery collected during the 2010 Eyjafjallajökull eruption. The similar acquisition channels of SLSTR and MODIS sensors and the comparable latitudes of the eruptions allow to extend the approach to SLSTR, thereby overcoming the lack in Sentinel-3 products collected in previous mid-high latitude eruptions. The results show that the neural network model is able to detect volcanic ash with good accuracy if compared with RGB visual inspection and BTM (Brightness Temperature Difference) procedures. Moreover, the comparison between the ash cloud obtained by the neural network (NN) and a plume mask manually generated for the specific SLSTR considered images, shows significant agreement. Thus, the proposed approach allows an automatic image classification during eruption events, and it is also considerably faster than time-consuming manual algorithms. Furthermore, the whole image classification indicates an overall reliability of the algorithm, in particular for recognition and discrimination from volcanic clouds.

## 30 **1 Introduction**

31 From the start of an eruptive event, volcanic emissions are composed of a broad distribution of ash particles, ranging from  
32 very fine ash (particle diameters,  $d < 30 \mu\text{m}$ ) increasing in size to tephra (airborne pyroclastic material) with diameters from 2  
33 mm up to 64 mm. Larger fragments are also generated which fall out quickly; these and ash with  $d > 30 \mu\text{m}$  are not considered  
34 in this paper. The gaseous part is made mainly of water vapour ( $\text{H}_2\text{O}$ ), carbon dioxide ( $\text{CO}_2$ ) and sulphur dioxide ( $\text{SO}_2$ ) gases  
35 (Oppenheimer et al., 2011; Shinohara, 2008), and also a liquid part consisting in sulphate aerosol is present. Depending on the  
36 eruptive intensity, the volcanic cloud can reach different altitudes in the atmosphere thus affecting environment (Craig et al.,  
37 2016; Delmelle et al., 2002), climate (Bourassa et al., 2012; Haywood & Boucher, 2000; Solomon et al., 2011), human health  
38 (Delmelle et al., 2002; Horwell et al., 2013; Horwell & Baxter, 2006; Mather et al., 2003) and aircraft safety (Casadevall,  
39 1994).

40 The detection procedure consists in identifying the presence of certain species in the atmosphere and discriminating them  
41 against other species. Thus, volcanic ash detection is related to the discrimination of the areas (pixels in an image), which are  
42 affected by the presence of these particles. First evidences about the possibility to detect volcanic cloud by means of remote  
43 sensing data arise in the eighties (A. J. Prata, 1989a; A. J. Prata, 1989b). The method used for the detection of volcanic ash  
44 particles relies on the ability to discriminate between volcanic clouds and meteorological ice and liquid water clouds by  
45 exploiting the different spectral absorption in the Thermal InfraRed (TIR) spectral range (7–14  $\mu\text{m}$ ). In this interval the  
46 absorption of ash particles with radius between 0.5  $\mu\text{m}$  and 15  $\mu\text{m}$  at wavelength of 11  $\mu\text{m}$  is larger than the absorption of ash  
47 particles at 12  $\mu\text{m}$ . The opposite happens for meteorological clouds, which absorb more significantly at longer TIR  
48 wavelengths. Therefore, the Brightness Temperature Difference (BTD), i.e. the difference between the Brightness  
49 Temperatures (BTs) at 11 and 12 microns, turns out to be negative ( $\Delta T_{11\mu\text{m}} - \Delta T_{12\mu\text{m}} < 0 \text{ } ^\circ\text{C}$ ) for regions affected by volcanic  
50 clouds and positive ( $\Delta T_{11\mu\text{m}} - \Delta T_{12\mu\text{m}} > 0 \text{ } ^\circ\text{C}$ ) for regions affected by meteorological clouds.

51 The BTD approach is the most used method for the volcanic cloud identification. It is effective and simple to apply, even if it  
52 can lead to false alarms in some cases, e.g. over clear surfaces during night, on soils containing large amounts of quartz (such  
53 as deserts), on very cold or ice surfaces, in the presence of high water vapour content (F. Prata et al., 2001). As already  
54 mentioned, the discrimination between volcanic and meteorological clouds is a challenging task, since the region of the overlap  
55 of the two objects shows a mixed behaviour not easily recognizable. In these mixed scenarios, the BTD can be negative not  
56 only for volcanic clouds but also for meteorological clouds; thus, some false positive results may occur, as the case of high  
57 meteorological clouds. False negative results may arise in the case of high atmospheric water vapour content: the water vapour  
58 contribution can hide and cancel out the ash particles effects on the BTD, and then the ashy pixels cannot be revealed. In these  
59 cases a correction procedure can be applied (Corradini et al., 2008, 2009; A. J. Prata & Grant, 2001). In addition to the described  
60 procedures, other algorithms have been developed (Francis et al., 2012; M. J. Pavolonis, 2010; M. Pavolonis & Sieglaff, 2012;  
61 Clarisse & Prata, 2016).

62 For these reasons, it seems appropriate to use advanced classification schemes to address the task of ash detection, such as  
63 approaches which make use of machine learning techniques, avoiding the need to find for each product the best BTD threshold  
64 for creating the volcanic cloud mask manually, which can be a time-consuming process.

65 For aerosol and meteorological cloud detection, a neural network (NN) (Atkinson & Tatnall, 1997; Bishop, 1994; Di Noia &  
66 Hasekamp, 2018) based algorithm allows the solution of a classification problem. Starting from inputs containing spectral  
67 radiance values acquired in a specific wavelength band, the model generates a prediction in output by assigning to each pixel  
68 of the original image a predefined class. In previous research, neural networks have already shown significant effectiveness in  
69 terms of atmospheric parameter extraction (Gardner & Dorling, 1998) and specifically for volcanic eruption scenarios (Gray  
70 & Bennartz, 2015; Picchiani et al., 2011, 2014; Piscini et al., 2014). A strong advantage of using a NN based approach for  
71 volcanic cloud detection is that once the model is trained on a statistically representative selection of test cases, new imagery  
72 acquired over new eruptions can be accurately (depending on the training phase) classified in near real time allowing significant  
73 advantages in critical situations and in emergency management.

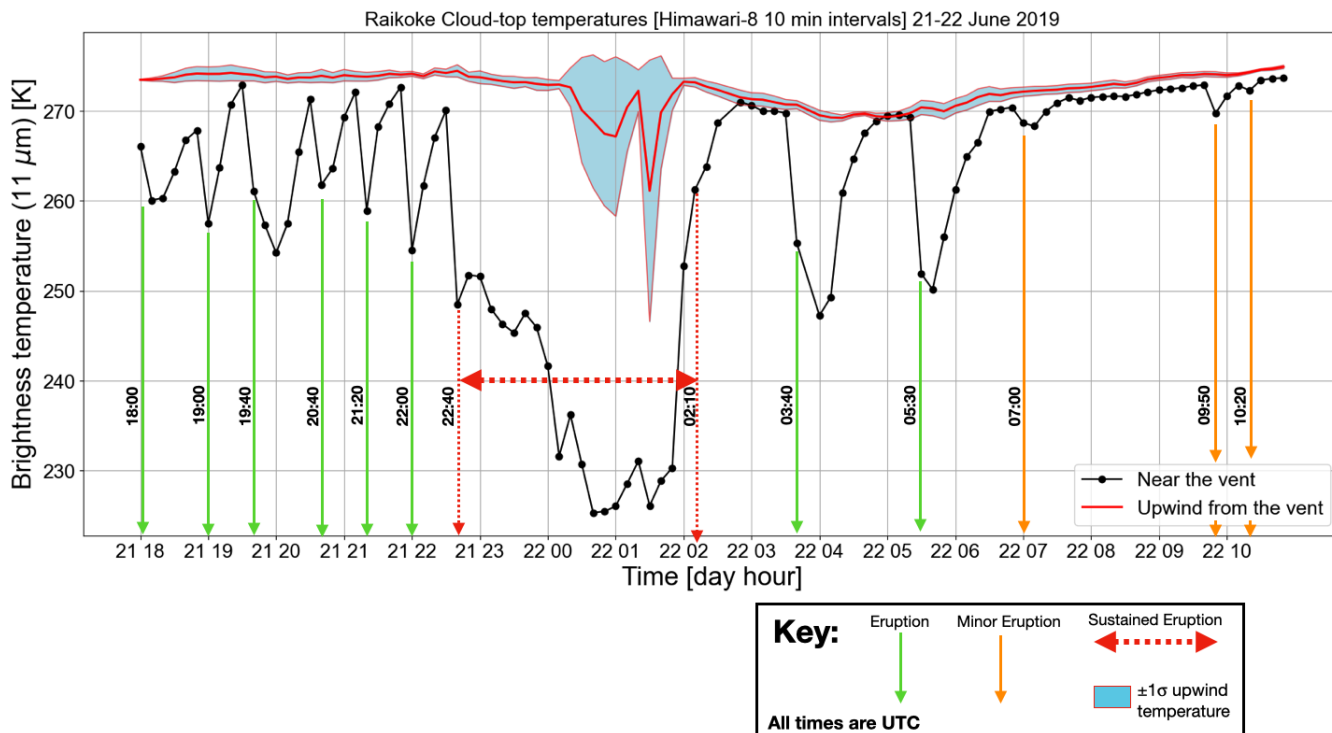
74 In this work, we developed a NN based algorithm for volcanic cloud detection using Sentinel-3 SLSTR (Sea and Land Surface  
75 Temperature Radiometer) daytime data with a model trained on MODIS (MODerate resolution Imaging Spectroradiometer)  
76 daytime images. This is possible since the two sensors have similar spectral bands and it represents an advantage as there is  
77 currently limited use of SLSTR products for eruptive events. The use of MODIS as a proxy for SLSTR was already successfully  
78 tested in a previous work investigating the complex challenge of distinguishing ice and meteorological clouds (also containing  
79 ice) using neural networks on SLSTR data (Picchiani et al., 2018). As a test case, the Raikoke 2019 eruption has been  
80 considered in this work.

## 81 **2 Case study: the Raikoke 2019 eruption**

82 The Raikoke volcano is located in the Kuril Island chain, near the Kamchatka Peninsula in Russia (48.3° N, 153.2° E). On  
83 June 21, 2019 at about 18:00 UTC Raikoke started erupting and continued erupting until about 03:00 UTC on 22 June 2019).  
84 During this period, Raikoke released large amount of ash and SO<sub>2</sub> into the stratosphere.

85 Figure 1 shows a time-series of 11 μm brightness temperatures (BTs) determined from the Himawari-8 AHI (Advanced  
86 Himawari Imager) sensor at 10-minute intervals for the first 18 hrs of the eruption. With the purpose of searching for high  
87 (cold) vertically ascending clouds due to an eruption, and not of meteorological origin, discrete eruptions were identified by  
88 comparing AHI BTs near the vent with those some distance upwind from the vent. The Himawari-8 time-series shows a  
89 sequence of eruptions (12 in all) and a sustained period of activity between 22:40 of 21 June and 02:10 of 22 June, when the  
90 majority of ash and gas was emitted. The estimated time of an eruption event was determined by examining animated images  
91 and consequently the times of eruptions shown do not always coincide with the coldest cloud-top. It is estimated from the  
92 AHI data that June 2019 Raikoke eruption produced approximately 0.4–1.8 Tg of ash (Bruckert et al., 2022; Muser et al.,  
93 2020; A. T. Prata et al., 2022) and 1–2 Tg of SO<sub>2</sub> (Bruckert et al., 2022; Gorkavyi et al., 2021). The amount of water vapour

94 emitted is unknown, but would have been considerable, as common in most volcanic eruptions (Glaze et al., 1997; McKee et  
 95 al., 2021; Millán et al., 2022; Murcay et al., 1981; Xu et al., 2022). These emissions would have led to copious amounts of  
 96 water and ice clouds being produced (McKee et al., 2021; Rose et al., 1995), making the composition of the transported clouds  
 97 both complex and changing with time.  
 98



99  
 100 **Figure 1:** Time-series of eruptions from Raikoke during the first 18 hrs of activity. The times of eruptions were estimated from the imagery  
 101 and do not always coincide with the coldest cloud tops. (Black line is the average within a box bounded by the latitude/longitude coordinates:  
 102 153.25-153.35°E, 48.32-48.42°N. The red line (upwind) is the average within a box bounded by: 153.10-153.20°E, 48.32-48.42°.

103  
 104 **3 Instruments**

105 In this section the specifications of the instruments which provide the products used to conduct the research are described. The  
 106 MODIS sensor on board Terra and Aqua satellites has been used to set up the training dataset of a NN based model. The  
 107 SLSTR sensor on board Sentinel-3A and Sentinel-3B satellites has been used for the application of the aforementioned model.

108 **3.1 MODIS instrument**

109 MODIS aboard NASA Terra and Aqua polar orbit satellites is a multispectral instrument, with 36 channels from VIS to TIR  
 110 ranging from 0.4 to 14.4  $\mu\text{m}$ , and spatial resolutions of 0.25 km for bands 1-2, 0.5 km for bands 3-7 and 1 km for bands 8-36.

111 The two spacecrafts fly at 705 km of altitude in a sun-synchronous orbit, with a revisit cycle of about one or two days. Terra  
112 spacecraft was launched in 1999 and its equatorial crossing time is 10:30 am (descending node), while Aqua was launched in  
113 2002 and its equatorial crossing time is 1:30 pm (ascending node).

114 In our work we used several Terra-Aqua/MODIS products: Level-1A Geolocation Fields (MOD/MYD03) (see (Nishihama et  
115 al., 1997) for details), Level-1B Calibrated Radiances (MOD/MYD021KM) (see (Toller et al., 2017) for details), which has  
116 been used to generate the Brightness Temperatures (BTs), Level-2 Surface Reflectance (MOD/MYD09) (see (Vermote &  
117 Vermeulen, 1999) for details), Level-2 Cloud Product (MOD/MYD06\_L2) (see (Menzel et al., 2015) for details).

### 118 **3.2 SLSTR instrument**

119 The Sea and Land Surface Temperature Radiometer (SLSTR) is one of the instruments on board the Sentinel-3A (S3A) and  
120 Sentinel-3B (S3B) polar satellites launched in 2016 and 2018, respectively.

121 Sentinel-3 is designed for a sun-synchronous orbit at 814.5 km of altitude with a local equatorial crossing time of 10:00 am.  
122 The revisit time is 0.9 days at equator for two operational spacecrafts configuration. The orbits of the two satellites are equal  
123 but S3B flies +/- 140° out of phase with S3A. The basic SLSTR technique is inherited from the technique used by the series  
124 of conical scanning radiometers starting with the ATSR. The instrument includes the set of channels used by ATSR-2 and  
125 AATSR (0.555 – 0.865 μm for VIS channels, 1.61 μm for SWIR channel, 3.74 – 12 μm for MWIR/TIR channels), ensuring  
126 continuity of data, together with two new channels at wavelengths of 1.375 and 2.25 μm in support of cloud clearing for surface  
127 temperature retrieval. The SLSTR radiometer measures a nadir and an along track scan, each of which also intersects the  
128 calibration black bodies and the visible calibration unit once per cycle (two successive scans). Each scan measures two along  
129 track pixels of 1 km (four or eight pixels at 0.5 km resolution for visible/NIR channels and SWIR channels, respectively)  
130 simultaneously. This configuration increases the swath width in both views, as well as providing 0.5 km resolution in the solar  
131 channels.

132 Our procedure makes use of the SLSTR Level-1 TOA (Top Of Atmosphere) Radiances and Brightness Temperature product  
133 from both platform S3A and S3B, see (Cox et al., 2021) for details of SLSTR Level-1 product.

134

### 135 **4 Methodology**

136 In this section the adopted methodology is described. The procedure has been developed in MatLab environment and the  
137 source codes are available upon request, as explained in Code Availability section. In particular, the MatLab Deep Learning  
138 Toolbox has been used to implement the NN.

139 A multilayer perceptron neural network (MLP NN) was trained with MODIS daytime data and then it was applied to Sentinel-  
140 3/SLSTR daytime products, in order to discriminate ashy pixels from others, following the scheme reported in Figure 2.

141 The MLP NN model (Atkinson & Tatnall, 1997; Gardner & Dorling, 1998) consists in a multi-layer architecture with three  
142 types of layers. The first type of layer is the input layer, where the nodes represents the elements of a feature vector. The second

143 type of layer is the hidden layer, and consists of only processing units. The third type of layer is the output layer and it represents  
 144 the output data, which are the classes to be distinguished and are set to one (that of the chosen class) or zero (all other nodes)  
 145 in image classification problems. All nodes (i.e. neurons) are interconnected and a weight is associated to each connection.  
 146 Each node in each layer passes the signal to the nodes in the next layer in a feed-forward way, and in this passage the signal is  
 147 modified by the weight. The receiving node sums the signals from all the nodes in the previous layer and elaborates them  
 148 through an activation function before passing them to the next layer.

149 The output of the proposed model is the SLSTR image fully classified in eight different species: ash over sea, ash over cloud,  
 150 ash over land, sea, land and ice surfaces, liquid water clouds and ice clouds. This approach has been used because of the readily  
 151 available time series of MODIS data, the quality of MODIS products (Picchiani et al., 2011, 2014; Piscini et al., 2014) and the  
 152 spatial/spectral similarities between MODIS and SLSTR. The SLSTR and MODIS channels which are used in our research  
 153 are shown in Table 1, along with the spectral characteristics of the two sensors.

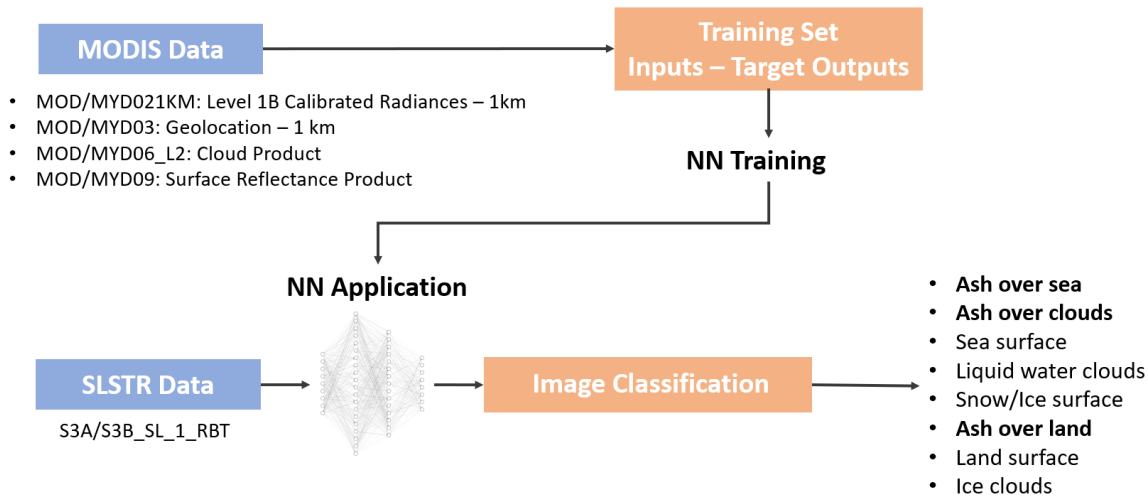
154 The first step of our procedure consists in generating the training patterns, that is the “ground truth” to be passed to the NN  
 155 model during the training phase. This step represents a crucial aspect in building a NN model since the more the training  
 156 dataset is accurate and representative of the problem we want to address the more the NN would be efficient in solving that  
 157 problem. For this scope, MODIS products have been used as inputs to a semi-automatic procedure for identifying the different  
 158 classes to be discriminated by the NN model in the output image. Some of these classes don’t exist as MODIS standard  
 159 products, for example the ash classes and the ice surface class; for this reason we derived them by means of different operations  
 160 in our semi-automatic procedure developed in MatLab. Other classes are instead already present as MODIS standard product,  
 161 for example the land/sea mask.

162

163 **Table 1:** Correspondence between MODIS and SLSTR channels.

<b>SLSTR Channel</b>	<b><math>\lambda</math> Centre (<math>\mu\text{m}</math>)</b>	<b>Bandwidth (nm)</b>	<b>MODIS Channel</b>	<b><math>\lambda</math> Centre (<math>\mu\text{m}</math>)</b>	<b>Bandwidth (<math>\mu\text{m}</math>)</b>
S1	0.554	19.26	4	0.555	0.545-0.565
S2	0.659	19.25	1	0.659	0.620-0.670
S3	0.868	20.60	2	0.865	0.841-0.876
S4	1.375	20.80	26	1.375	1.360-1.390
S5	1.61	60.68	6	1.64	1.628-1.652
S6	2.25	50.15	7	2.13	2.105-2.155
S7	3.74	398.00	20	3.75	3.660-3.840
S8	10.85	776.00	31	11.03	10.780-11.280
S9	12.02	905.00	32	12.02	11.770-12.270

164



166

167 **Figure 2:** Overall diagram of the procedure followed for the classification process with NN model.

168 The training set from which we extracted the training patterns (i.e. identifying classification classes) consists of nine MODIS  
 169 granules acquired over the Eyjafjallajökull volcano area during the 2010 eruption (from May 6<sup>th</sup> to May 13<sup>th</sup>), for a total of  
 170 about 5400 patterns for each class available for the training of the model. The single training pattern (i.e.: training example)  
 171 corresponds to a single pixel of a specific target class as identified in MODIS images through the semi-automatic procedure  
 172 aforementioned, this means that one class is represented by several patterns. In particular, not all the pixels of the considered  
 173 MODIS images are contained in the training dataset (i.e.: the ensemble of the training patterns), but only a part of them are  
 174 randomly included. The total number of patterns we collected has been divided into three subsets: 75% training set, 20%  
 175 validation set, 5% test set. A NN with two hidden layers of was trained and then it was applied to Sentinel-3 SLSTR RBT  
 176 (Radiance and Brightness Temperature) Level 1 images collected during the Raikoke 2019 eruption. Table 2 shows the details  
 177 of MODIS and SLSTR data used for this work.

178

179 **Table 2:** Training set (MODIS) from the Eyjafjallajökull 2010 eruption; Sentinel-3 Raikoke 2019 classified products.

Date	Time UTC	Platform	Training/Application
6 May 2010 (JD 126)	11:55	Terra	Training
9 May 2010 (JD 129)	12:25	Terra	Training
11 May 2010 (JD 131)	12:10	Terra	Training
11 May 2010 (JD 131)	12:15	Terra	Training
11 May 2010 (JD 131)	13:50	Terra	Training
11 May 2010 (JD 131)	14:05	Aqua	Training
12 May 2010 (JD 132)	12:55	Terra	Training

13 May 2010 (JD 133)	12:00	Terra	Training
13 May 2010 (JD 133)	13:40	Terra	Training
22 June 2019 (JD 173)	00:07	Sentinel-3A	Application
22 June 2019 (JD 173)	23:01	Sentinel-3B	Application

180

181 In order to build the NN training patterns a semi-automatic procedure, that exploits MODIS radiances and standard products,  
 182 has been developed. The MODIS products considered for the extraction of the training patterns are the following:

- 183 • MOD/MYD021KM, Level 1B Calibrated Radiances – 1 km, which gives the radiance values for each MODIS band;
- 184 • MOD/MYD03, Geolocation – 1 km, used for creating the Land/Sea Mask;
- 185 • MOD/MYD06\_L2, Cloud Product, containing cloud parameters, used for creating the Cloud Mask;
- 186 • MOD/MYD09, Surface Reflectance Product, containing an estimate of the surface spectral reflectance measured at  
 187 ground level; it is used for generating the Ice Mask;

188 where “MOD” and “MYD” stands for MODIS-Terra and MODIS-Aqua products respectively.





189 The semi-automatic procedure for the extraction of training patterns starting from MODIS data basically consists in using  
 190 MODIS products to create binary “masks” identifying the different species, and then replaces them by “classes”. For each  
 191 element of the class the radiance values ( $W/(m^2 sr \mu m)$ ) are extracted from the MODIS product MOD/MYD021KM. In this  
 192 way each object is radiometrically characterized. The identification of the ashy pixel is pursued by creating a mask according  
 193 to specific BTD thresholds (from 0.0 to -0.4 °C) for each MODIS image. For this purpose, the MOD/MYD021KM product  
 194 has been used to derive the brightness temperatures required to compute the BTD. The MODIS products used for training the  
 195 model were acquired in near-nadir view only.

196 The other species are identified using both MODIS Level 1 radiances and MODIS standard products. Once each object/surface  
 197 has been defined, they are associated with the corresponding class. Then a set of input-output samples for the training phase is  
 198 generated, where the input consists of the set of radiances measured for the given pixel and the output is a binary vector with  
 199 value 1 associated with the corresponding class and value 0 for the other classes.

200 Table 3 shows the classification map legend for each classified product presented in this work, in which eight classes are  
 201 discriminated, each one representing a surface/object.

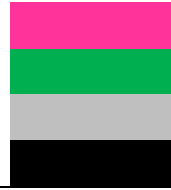
202

203 **Table 3:** Classification map legend.

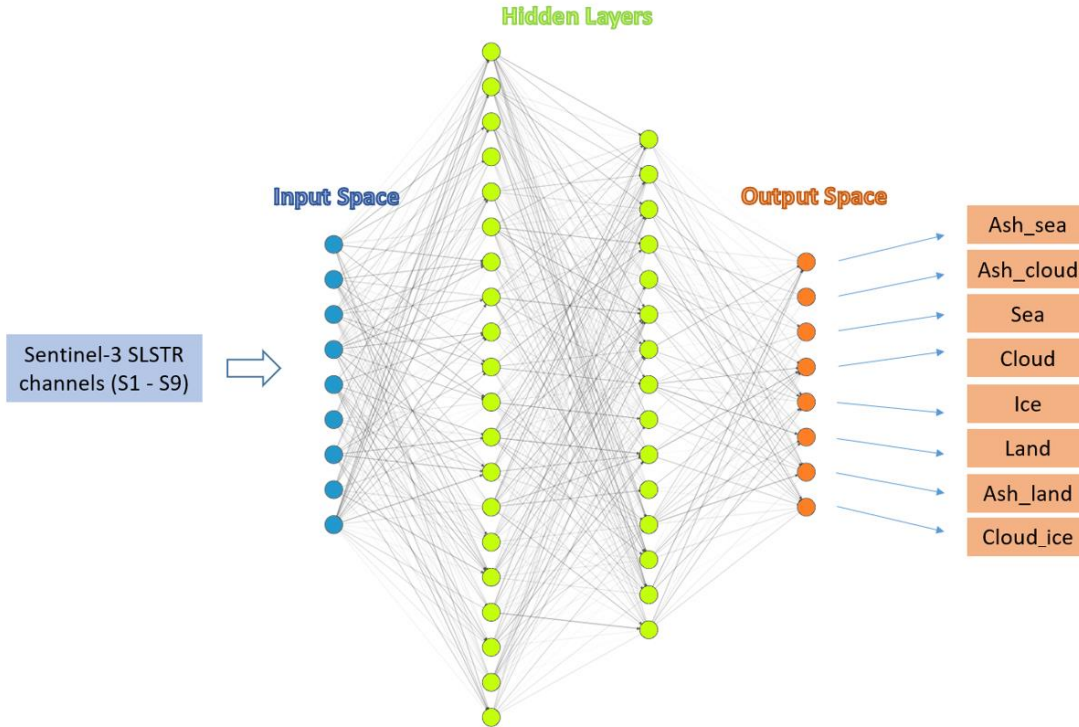
Class ID	Surface/Object	Name	Colour
1	Ash over sea	<i>Ash_sea</i>	
2	Ash over clouds	<i>Ash_cloud</i>	
3	Sea surface	<i>Sea</i>	
4	Liquid water clouds	<i>Cloud</i>	



5	Snow/Ice surface	<i>Ice</i>	
6	Ash over land	<i>Ash_land</i>	
7	Land surface	<i>Land</i>	
8	Ice clouds	<i>Cloud_ice</i>	
-	Masked out pixels	<i>Not classified</i>	



204

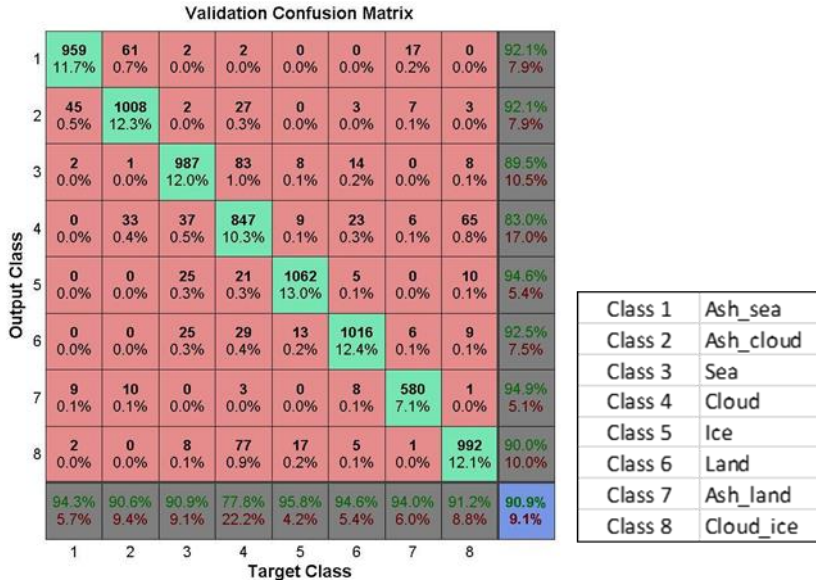


205

206 **Figure 3:** NN topology for ash detection.

207 The NN final model consists of nine inputs, which are the radiances in the SLSTR selected channels, while the output space  
 208 is composed of eight classes, which are the objects/surfaces which the net has to classify. After doing several tests the optimum  
 209 topology of the NN turns out to be the combination of two hidden layers with 20 and 15 neurons, respectively. For each neuron  
 210 we set the hyperbolic tangent activation function (Vogl et al., 1988). The final neural network architecture used for ash  
 211 detection in this work is shown in Figure 3. The proposed algorithm includes a post processing operation in order to avoid  
 212 false positive results for land and sea classes. This *a-posteriori* filter is applied both to the resulting NN land and sea classes.  
 213 It allows masking out the pixels which the NN classifies as land/sea which do not belong to the Sentinel-3/SLSTR land/sea  
 214 mask standard product, which is always available and thus it can be used to increase the precision of the algorithm. The filtered  
 215 out pixels have been inserted in a class named “not classified”, as reported in Table 3.

216 For classification problems approached with machine learning algorithms, one of the most used accuracy metrics for the  
 217 performance evaluation is the confusion matrix (Fawcett, 2006), where each predicted output class is compared to the  
 218 corresponding ground truth considered in the validation dataset. An overall accuracy of 90.9% was obtained at the end of the  
 219 NN training phase for the proposed neural network model (see Figure 4).  
 220



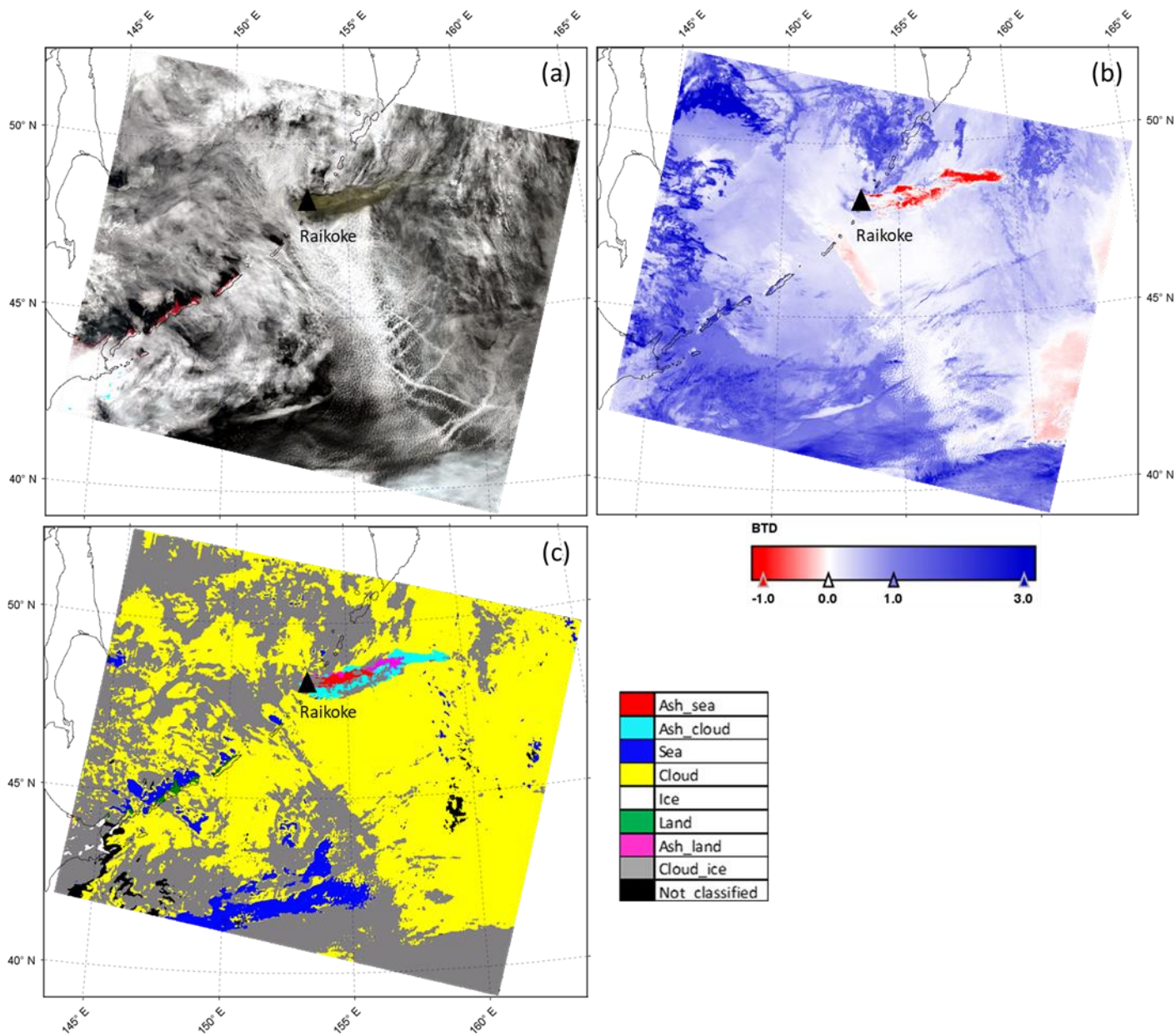
221  
 222 **Figure 4:** Confusion matrix on validation set.

223 The target class represents the “ground truth” of each class, while the output class refers to the prediction of the NN. The  
 224 diagonal shows that most of the total of the pixels have been correctly classified (green boxes). The number of pixels incorrectly  
 225 classified are placed out of the diagonal. False positives (false detection) and false negatives (missed detection) are reported  
 226 in the last grey column and row, respectively.

227 The code of the procedure ran with a CPU i7-9850H (6 core, processor base frequency at 2.60 GHz): it takes less than 30  
 228 minutes to train the adopted model and few seconds to apply it.

229 **5 Results and Discussion**

230 The neural network algorithm previously described was applied to Sentinel-3/SLSTR daytime images acquired on Raikoke  
 231 during the 2019 eruption. The Sentinel-3A/SLSTR and Sentinel-3B/SLSTR products collected on 22 June 2019 at 00:07 and  
 232 23:01 UTC have been considered (see Table 2).

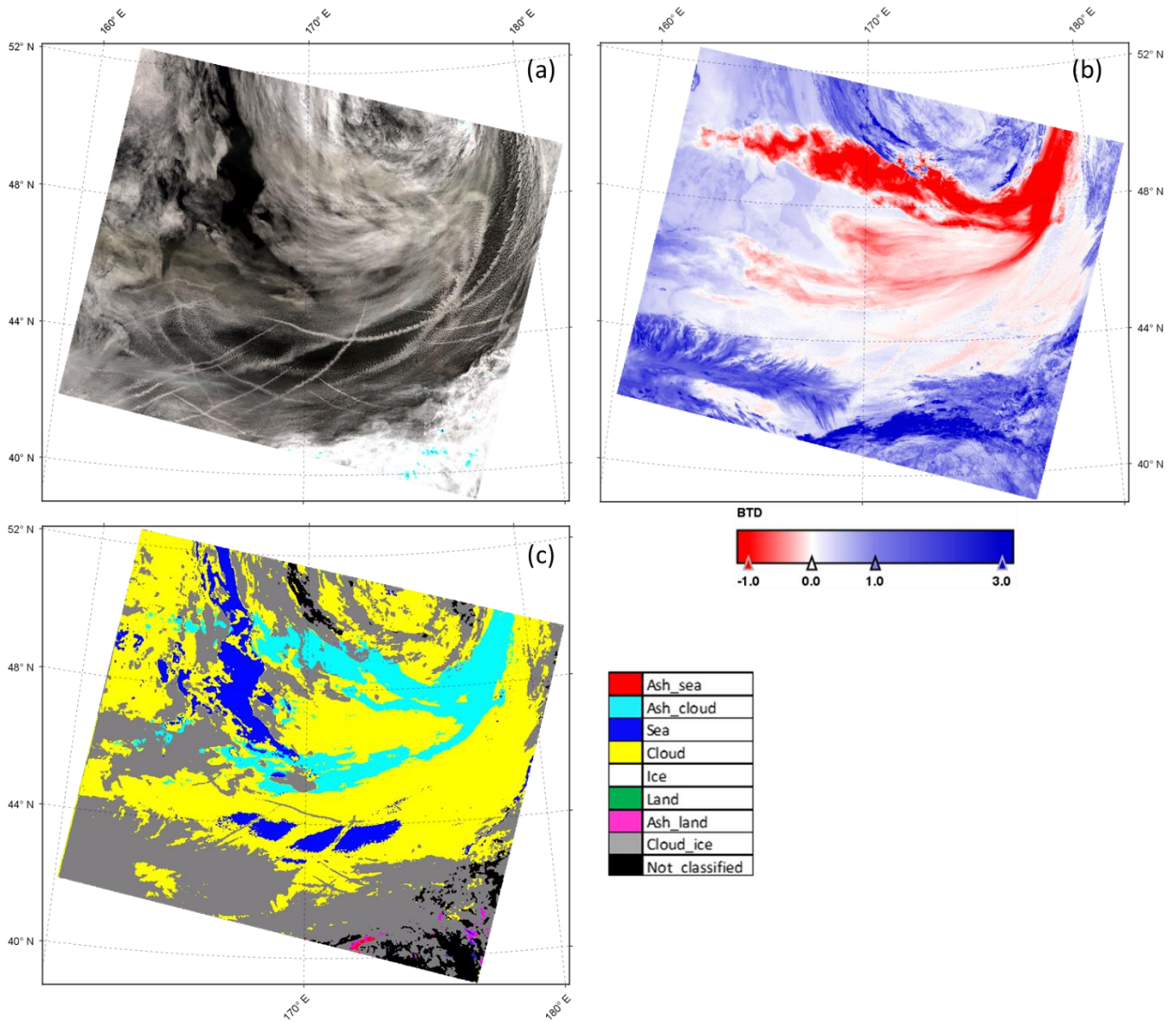


233

234 **Figure 5:** Sentinel-3A/SLSTR image collected on Raikoke for 22 Jun 2019 at 00:07 UTC, nadir view. (a) RGB; (b): BTD; (c): NN  
 235 classification.

236 Figure 5(a) shows the RGB colour composite of the S3A/SLSTR image acquired on Raikoke for 22 June 2019 at 00:07 UTC.  
 237 The RGB composite has been carried out by considering the SLSTR visible (VIS) channels S3 (868 nm), S2 (659 nm) and S1  
 238 (554 nm) for R, G and B, respectively. In Figure 5(b) the BTD map is displayed, where red and blue pixels represent negative  
 239 and positive BTD, respectively. The BTD is computed by making the difference between the brightness temperature of the

240 SLSTR thermal infrared channels S8 and S9 centred at 10.8 and 12  $\mu\text{m}$ . The output of the NN classification is shown in Figure  
 241 5(c) with the corresponding colour legend, where each colour represents the classified surface/object.



242  
 243 **Figure 6:** Sentinel-3B/SLSTR image collected on Raikoke for 22 June 2019 at 23:01 UTC, nadir view. (a): RGB; (b): BTB; (c): NN  
 244 classification.

245 As Figure 5(a) shows, the RGB composite shows the presence of a wide distribution of meteorological clouds and a significant  
 246 signal derived from the volcanic cloud (brown pixels). The BTB (Figure 5(b)), obtained with a threshold of 0  $^{\circ}\text{C}$ , shows the  
 247 presence of the volcanic cloud together with a significant number of false negatives (volcanic cloud pixels not identified near

248 the vents) and false positives (pixels identified as volcanic cloud while actually they are not, see light red pixels below the  
249 volcanic cloud and along the right edge of the scene).

250 Despite the challenging scenario, the NN algorithm shows its ability to detect the volcanic cloud and to classify the whole  
251 image, by detecting with good accuracy meteorological clouds composed of water droplets (yellow) and ice (grey), sea (blue)  
252 and land (green) surfaces, and volcanic ash clouds, as reported in Figure 5(c). Looking at the cloud masks generated with the  
253 NN algorithm (yellow and grey) and by comparing them with the RGB natural colour composite of the SLSTR product, a high  
254 degree of agreement in terms of spatial features can be observed. From the comparison between NN output classes and RGB  
255 composite we can observe that also land (green) and sea (blue) pixels are properly detected in the areas where they actually  
256 lie.

257 From a qualitative comparison between the NN plume mask and the RGB composite, we can state that the NN correctly  
258 identifies the volcanic cloud class in the area where it seems actually present, even if some pixels are misclassified as ash over  
259 land (magenta pixels), instead of ash above meteorological cloud. As Figure 5 shows, the NN algorithm is able to detect a  
260 wide volcanic cloud area and more ash, especially in the opaque regions, compared to the BTD approach. In particular the  
261 difference found near the vents can be due to the complete opacity of the cloud. Here the ash cloud optical thickness is so high  
262 that there is no spectral difference and the BTD approach has no sensitivity.

263 Following the same visualization scheme of Figure 5, the results derived from the application of the trained NN model to the  
264 S3B/SLSTR image acquired on 22 June 2019 at 23:01 UTC are reported in Figure 6. In this second image, all the ashy pixels  
265 are classified by the NN model as ash above meteorological clouds (cyan pixels). This seems reasonable being the scenario  
266 mostly dominated by meteorological clouds, as we can also observe looking at the NN classification, which assigns the  
267 majority of the pixels to the liquid water cloud class (yellow) and to the ice cloud class (grey). The NN classification shows  
268 also the presence of sea pixels (blue), which are located in the same area identifiable using the RGB composite. In this case,  
269 from the RGB composite (Figure 6(a)), unlike what is seen in the 00:07 UTC image, it is not straightforward to identify the  
270 volcanic plume by visual inspection. Indeed, this image was collected about 24 hours later than the previous one and thus the  
271 plume has been transported through the atmosphere and dispersed. A qualitative comparison between the NN classification  
272 (Figure 6(c)) and the BTD map (Figure 6(b)) shows considerable differences between the two methods. The BTD, obtained  
273 with a threshold of 0 °C, identifies a wider area (red pixels) affected by the volcanic cloud with respect to the NN ash mask  
274 (cyan pixels). We can notice that the BTD map includes some aircraft condensation trails (recognizable by the shape in the  
275 RGB composite) in the ash mask, which can be identified as false ash detections. The reasons for these misclassifications are  
276 not fully understood, but may be due to multilayer cloud effects, pixel heterogeneity or viewing angle.

277 Our results suggest that the NN technique is robust and has shown that it is possible to transfer the NN model from one single  
278 eruption event to others occurring at similar latitudes. However, the complexity of the application suggests that the  
279 generalization of the methodology to all types of eruptions is not straightforward. For example, the change of latitude has an  
280 impact on the characteristics of the atmosphere. At the same time different volcanoes emit different types of ash affecting the

281 variability of the radiance values detected by the sensors. A possible solution to give to the proposed technique a broader  
 282 applicability could be training different NN models for specific latitude belts which can be defined to cover the whole globe.  
 283 Overall, we can summarize the main uncertainties and the limitations of the presented model in the following points:

- 284 1. model transferability is significantly related to the spatial-temporal data availability for the generation of a training  
 285 dataset which is statistically representative of all the possible scenarios;
- 286 2. lack of standard ground truth data for training and validation phases requires the BTD threshold selection by an  
 287 operator which prevents the method from being fully objective.

## 288 5.1 Vicarious validation

289 The capability of the NN to correctly detect pixels containing ash was validated by making a pixel per pixel comparison with  
 290 a reference plume mask generated manually (hereafter MPM) in order to obtain the best accurate *ground truth* as possible in  
 291 each SLSTR product. The choice of taking the MPM as reference derives from the lack of ash standard products.

292 For the image collected at 00:07 UTC the MPM creation was performed by selecting a region around the volcanic cloud  
 293 (clearly recognizable as it is at the beginning of the eruption) and then considering only the pixels with 11  $\mu\text{m}$  brightness  
 294 temperature  $< 270\text{ K}$  (see Figure 1). In this case the BTD alone it is not very useful as the high value of the ash optical thickness  
 295 of the cloud (especially close to the vent) produces many pixels with BTD values near zero, not distinguishable from adjacent  
 296 pixels characterized by meteorological clouds. For the image collected at 23:01 UTC, the identification of the volcanic cloud  
 297 is much more difficult due to its larger spread and dilution; in this case the MPM was obtained considering the pixels with  
 298 BTD  $< -0.25\text{ }^\circ\text{C}$ , even if probably this choice implies that some ashy pixels were discarded. On the other hand, using an higher  
 299 BTD threshold will produce a lot of false positive pixels. In general, the creation of an accurate manual plume mask is time  
 300 consuming and case-sensitive and often requires the presence of an operator; so the generation of a volcanic cloud mask with  
 301 a fast, automatic and case-independent procedure would be a rather significant improvement.

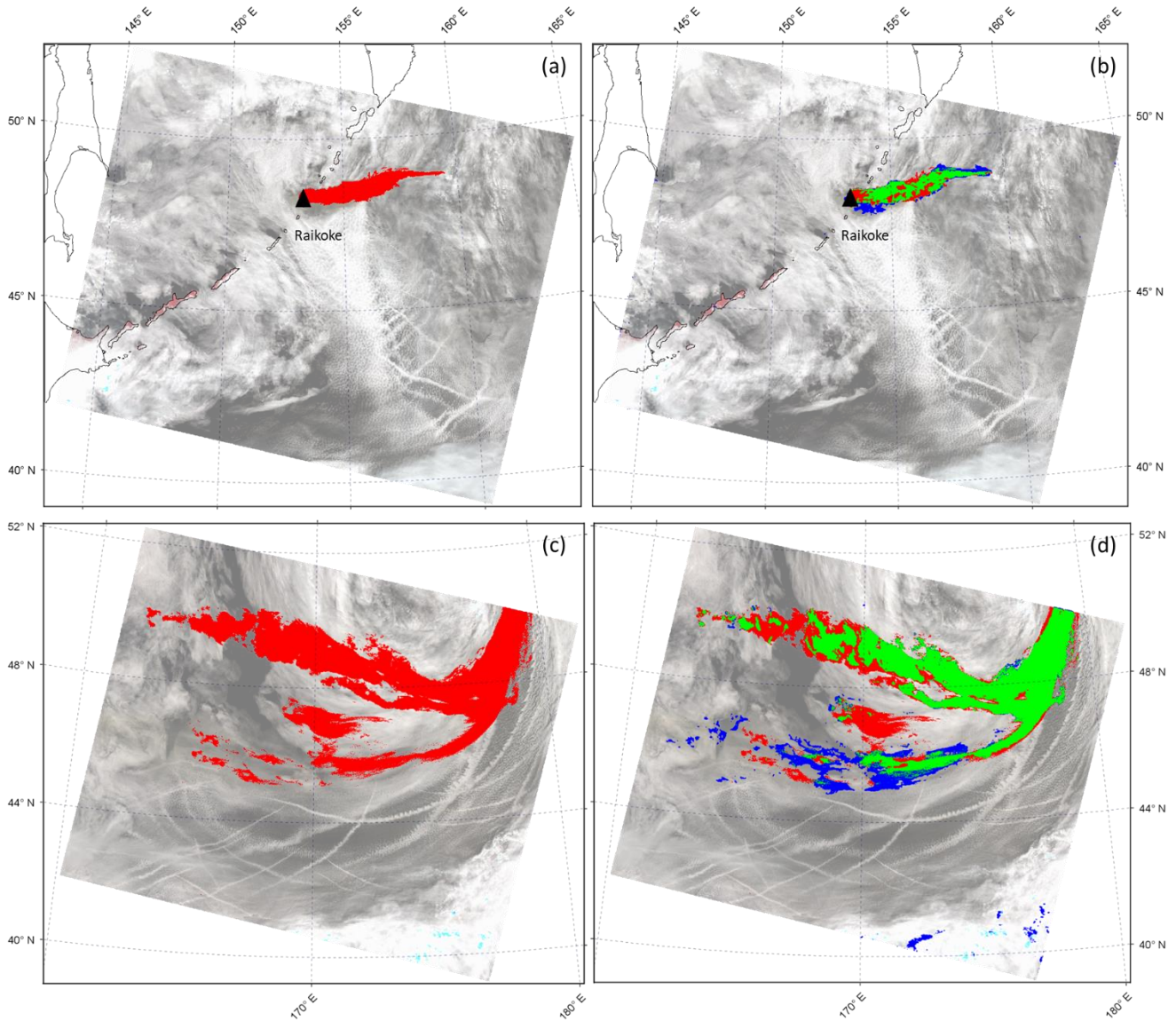
302 Because the MPM doesn't distinguish between the different surfaces under the ash cloud, the validation is performed by  
 303 considering the total of the ashy pixels detected from the NN (i.e. the sum between *ash\_land*, *ash\_sea* and *ash\_cloud*).

304 Figure 7 shows the MPM, created as described above, and the comparison between NN plume mask (hereafter NNPM) and  
 305 MPM for the S3A/SLSTR image collected on Raikoke for 22 June 2019 at 00:07 UTC (Figure 7(a) and Figure 7(b)) and  
 306 S3B/SLSTR image collected on Raikoke for 22 June 2019 at 23:01 UTC (Figure 7(c) and Figure 7(d)).

308 **Table 4:** NN and BTD volcanic cloud detection accuracies using classification metrics derived from the comparison between the plume  
 309 mask obtained from the two approaches and the manual plume mask (MPM) for each SLSTR considered product, respectively.

Classified Product	Plume mask source	Precision	Recall	F-measure	Accuracy
S3A/SLSTR at 00:07 UTC	NN classification	0.709	0.683	0.696	0.993
S3A/SLSTR at 00:07 UTC	BTD $< 0\text{ }^\circ\text{C}$	0.164	0.647	0.261	0.955
S3B/SLSTR at 23:01 UTC	NN classification	0.773	0.657	0.710	0.935

310



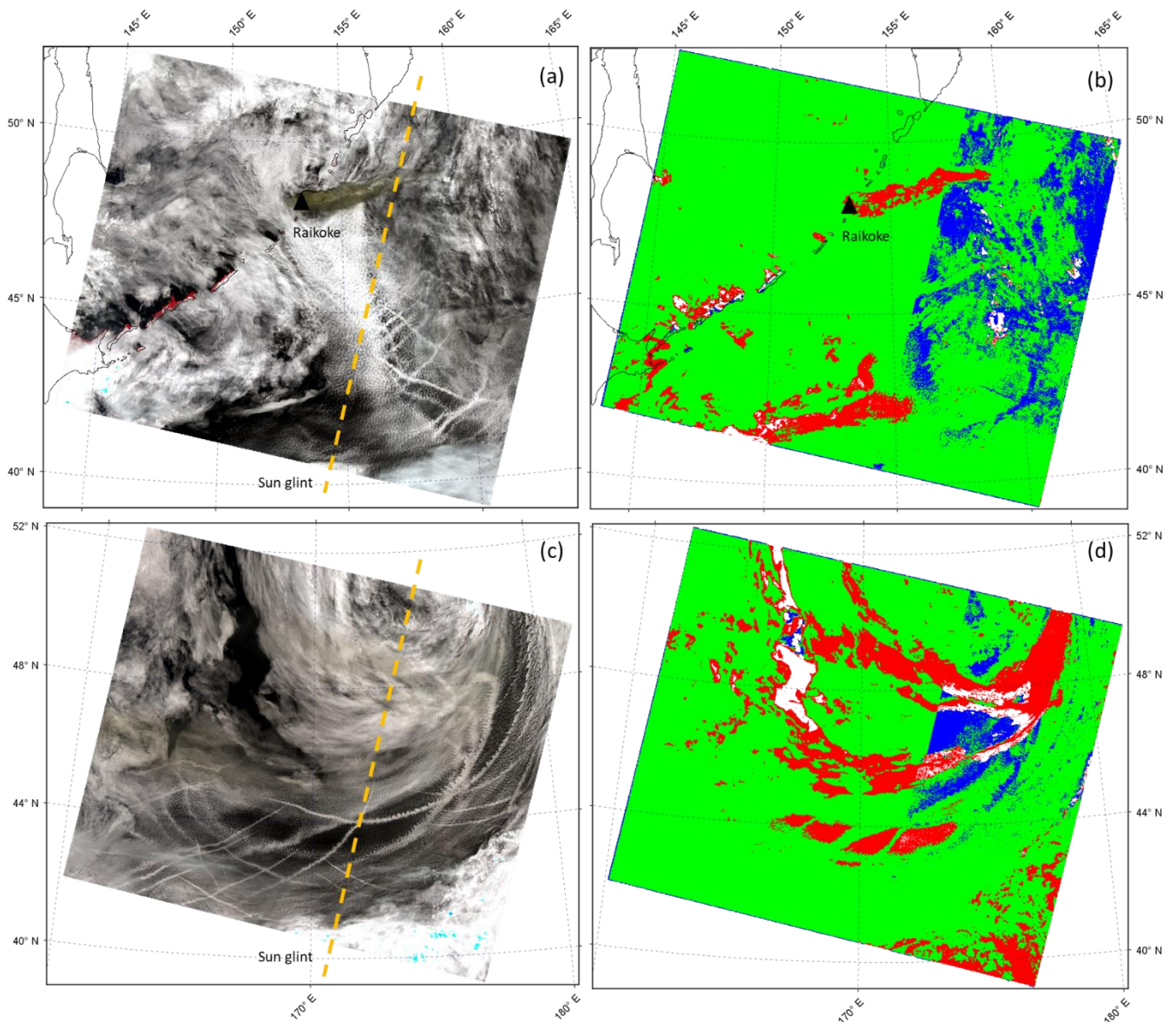
311

312 **Figure 7:** Sentinel-3A/SLSTR image collected on Raikoke for 22 June 2019 at 00:07, nadir view (a),(b); Sentinel-3B/SLSTR image collected  
313 on Raikoke for 22 June 2019 at 23:01, nadir view (c),(d). (a),(c): red pixels display the manual plume mask (MPM) obtained from the  
314 analysis on the specific image; (b),(d): comparison between volcanic ash detected by NN and MPM; green pixels indicate the areas for which  
315 both NN and MPM detect ashy pixels, red pixels indicate the areas for which only MPM detects ashy pixels, blue pixels indicate the areas  
316 for which only NN detects ashy pixels.

317

318

319



320

321 **Figure 8:** Sentinel-3A/SLSTR image collected on Raikoke for 22 June 2019 at 00:07, nadir view (a),(b); Sentinel-3B/SLSTR image collected  
 322 on Raikoke for 22 June 2019 at 23:01, nadir view (c),(d). (a),(c): RGB view; (b),(d): comparison between cloud mask retrieved by NN and  
 323 standard Sentinel-3 confidence in summary cloud mask (CSCM); green pixels indicate the areas for which both NN and CSCM detect cloudy  
 324 pixels, red pixels indicate the areas for which only CSCM detects cloudy pixels, blue pixels indicate the areas for which only NN detects  
 325 cloudy pixels, white pixels indicate the areas for which both NN and CSCM don't detect cloudy pixels.

326

327 In relation to the images which display the comparison between NN output and MPM (Figure 7(b) and Figure 7(d)), green  
 328 areas indicate the pixels for which both the MPM and NN ash masks detect the presence of volcanic cloud, red pixels represent  
 329 the areas classified as ash only by the MPM; blue pixels are classified as ash only according to the NN model. We can observe



330 that most of the volcanic cloud is displayed in green for both products (00:07 UTC and 23:01 UTC), indicating good agreement  
 331 between the two approaches. This is also confirmed by the scores in Table 4, which allow quantitative conclusions on the  
 332 accuracy of the proposed NN model approach compared to the MPM considered as *ground truth*. The classification metrics  
 333 considered are precision, recall, F-measure and accuracy (Fawcett, 2006) which range from 0 to 1 (perfect classifier).

334 The score differences for the two classified products are mainly related to the significant higher number of correctly classified  
 335 ashy pixels contained in the 23:01 UTC (136435 pixels) with respect to 00:07 UTC (13545 pixels), if compared to the total  
 336 number of classified pixels in the images which is similar (1614405 pixels for the S3A/SLSTR at 00:07 UTC image and  
 337 1701319 for the S3B/SLSTR at 23:01 UTC image respectively). However, the metrics are aligned for both classified data with  
 338 encouraging values for each index suggesting the reasonability of the results. In particular, the F-measure results of around 0.7  
 339 for both classifications. Moreover, using MPM as a benchmark, the comparison of the metrics obtained with the  $BTD < 0^{\circ}C$   
 340 approach with those derived with the NN model indicates that the neural network performs a more accurate volcanic cloud  
 341 detection for both considered test cases.

342 Besides the NN plume mask validation, we also compared the pixels which the NN model classified as affected by  
 343 meteorological clouds (hereafter NNCM) with the SLSTR standard product for meteorological clouds.

344 Among the cloud masks available in the SLSTR L1RBT product, the *confidence\_in\_summary\_cloud* mask (hereafter CSCM)  
 345 is considered. The CSCM is a cloud mask which discriminates cloud pixels (*true*) and cloud-free pixels (*false*); it is an ultimate  
 346 cloud mask product derived from several separated cloud tests (Polehampton et al., 2021). As the CSCM doesn't distinguish  
 347 between meteorological liquid water clouds and meteorological ice clouds as the NN algorithm does, the comparison is realized  
 348 by considering the whole NN meteorological cloud classes (i.e. the sum between *Cloud* and *Cloud\_ice*).

349 Figure 8 displays the RGB composite, in which the Sentinel-3 sun glint mask is highlighted (right part of the scene), and the  
 350 comparison between NN cloud mask and S3 cloud mask for S3A/SLSTR image collected on Raikoke for 22 June 2019 at  
 351 00:07 UTC (Figure 8(a) and Figure 8(b)) and for S3B/SLSTR image collected on Raikoke for 22 June 2019 at 23:01 UTC  
 352 (Figure 8(c) and Figure 8(d)).

353 Also in this case, for the images displaying the comparison between the two types of cloud masks (Figure 8(b) and Figure  
 354 8(d)), green indicates the pixels classified as meteorological cloud for both procedures, while red and blue indicate the pixels  
 355 classified as meteorological cloud only from the SLSTR standard product and NN, respectively. Pixels that are not coloured  
 356 are associated to a cloud-free condition for both the NN and the S3 cloud mask. Looking at the comparison, a very good  
 357 agreement between the NN meteorological cloud mask and the SLSTR standard cloud mask can be observed. The metrics in  
 358 Table 5 show very good performances, reaching an F-measure around 0.9. Moreover, looking at the red pixels in the 23:01  
 359 UTC image especially, it can be noted that the SLSTR cloud mask also includes the volcanic cloud.

360

361 **Table 5:** NN meteorological cloud detection accuracy using classification metrics derived from the comparison between the NN cloud mask  
 362 (NNCM) and the confidence in summary cloud mask (CSCM) for each SLSTR considered product which has been assumed as ground truth.

Classified Product	Precision	Recall	F-measure	Accuracy
--------------------	-----------	--------	-----------	----------

S3A/SLSTR at 00:07 UTC	0.891	0.936	0.913	0.842
S3B/SLSTR at 23:01 UTC	0.952	0.820	0.881	0.795

363

364 From the validation procedure we have carried out, a considerable point which has to be underlined is that, unlike adopting a  
365 time consuming and case-specific approach as MPM which also needs a manual operation by setting various thresholds for  
366 each case under examination, the NN model can be used to discriminate ash plume in satellite images with good accuracy in  
367 a fast and automatic way, which saves a significant amount of time by eliminating the need for manual intervention.

368

## 369 **6 Conclusions**

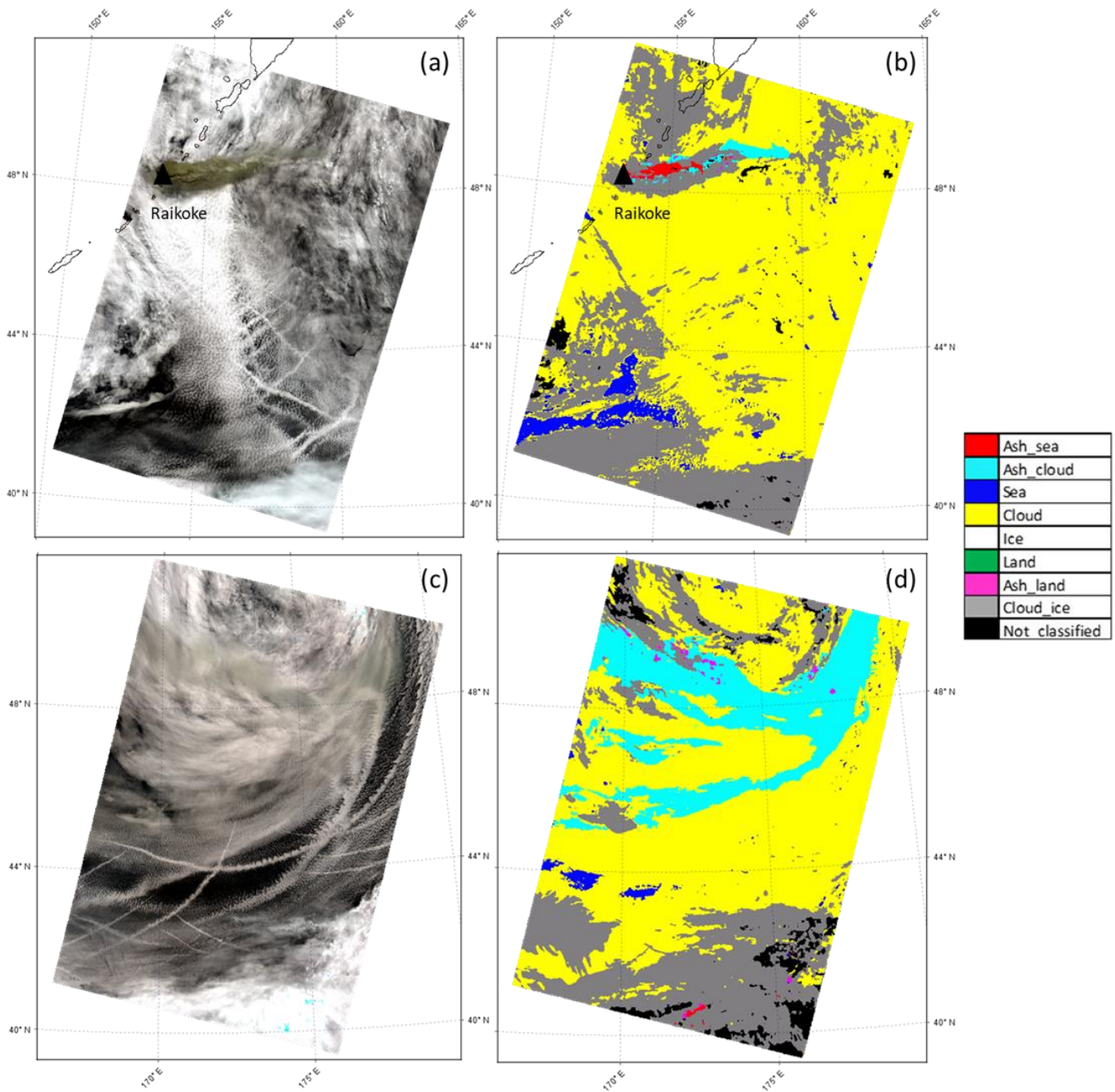
370 In this work the results of a new neural network based approach for volcanic cloud detection are described. The algorithm,  
371 developed to process Sentinel-3/SLSTR daytime images, exploits the use of MODIS daytime data as training. The procedure  
372 allows the full characterization of the SLSTR image by identifying, besides the volcanic cloud, surfaces under the cloud itself,  
373 meteorological clouds (and phases), land, and sea surfaces. As test cases, the S3A-S3B/SLSTR images collected over the  
374 Raikoke volcano area during the June 2019 eruption have been considered.

375 The proposed neural network based approach for volcanic ash detection and image classification shows an overall good  
376 accuracy for the ash class, which is the main target of the algorithm, and for the meteorological cloud class as well. A strong  
377 effectiveness of the NN classification is indeed also related to the cloudy pixel recognition, with the ability to distinguish two  
378 different types of meteorological clouds composed of water droplets and ice respectively. It has to be reminded that the wide  
379 distribution of meteorological clouds in the scenario under consideration makes the ash detection task particularly complex.  
380 A point to be underlined is the valuable advantage of the procedure related to the creation of products (the eight classes) not  
381 all currently available as SLSTR standard products; this fact represents a considerable step forward for generation of novel  
382 types of S3/SLSTR products.

383 A post processing has been applied to NN outputs by exploiting the land/sea mask available in the SLSTR standard products,  
384 in order to mitigate the insurgence of NN land/sea failure.

385 The comparison between the NN plume mask and a reference plume mask (MPM) taken as *ground truth*, shows a good  
386 agreement between the two techniques. The significant result lies in the fact that the overall good performance of the NN  
387 output is achieved in an automatic way and with a brief processing time, compared to the plume mask specifically generated,  
388 which instead requires a longer time, is case-specific and needs the presence of an operator. The other considerable  
389 achievement of the NN developed procedure is that, once the NN model has been properly trained, it has been used to detect  
390 the ash plume for each SLSTR image related to the Raikoke eruption, while the creation of the MPM has to be made separately  
391 for each image.

392 The comparison between the NN cloud mask and the cloud mask derived from SLSTR standard products has also been carried  
393 out, resulting in a high percentage of agreement between the two products.



394

395 **Figure 9:** Sentinel-3A/SLSTR image collected on Raikoke for 22 Jun 2019 at 00:07 UTC, oblique view ((a) and (b)); Sentinel-3B/SLSTR  
 396 image collected on Raikoke for 22 June 2019 at 23:01 UTC, oblique view ((c) and (d)). (a) and (c): RGB; (b) and (d): NN classification.

397 A promising outcome is related to the ability of the NN model to generalize over different data in terms of spatio-temporal and  
 398 geographical characteristics, being the NN model trained with data collected over the Iceland region in 2010 and then applied  
 399 to data acquired over the Kamchatka Peninsula in Russia in 2019. Something under consideration for future improvements is

400 to enhance the ability of the NN to generalize over various eruptive scenarios, by integrating different training dataset (in terms  
401 of regions, type of eruption, time interval, etc). In fact, the current methodology has been applied just to a few test cases and  
402 more validation is required in order to give the technique broader applicability. For example, the effects of varying moisture  
403 and atmospheric conditions has not been fully explored. On the other hand, the generation of an appropriate number of  
404 examples, which must be statistically representative of all the possible scenarios, to be included in the training dataset may  
405 represent a very difficult task. A possible approach could be the design of different neural networks, each associated with a  
406 specific scenario.

407 We also aim at further investigate some aspects in order to improve the classification accuracy, as the introduction of other  
408 output classes, such as volcanic ice cloud, and the integration of other variables in the model, such as the sensor view angle.  
409 Moreover, a fully comprehensive study about the sensitivity of the NN detection on the observation angle could be another  
410 possible future development of the study. Here we addressed briefly this point applying the trained network to SLSTR oblique  
411 view products, characterized by a zenith view angle of about  $55^\circ$  (Polehampton et al., 2021). shows the RGB composite and  
412 the NN classification for the SLSTR oblique view product collected on 22 June 2019 at 00:07 UTC ((a) and (b)) and 23:01  
413 UTC ((c) and (d)) respectively. It is interesting, as a preliminary result, to show how, especially for the 23:01 UTC image  
414 where the opacity of the volcanic cloud is slighter, the main features of the classification map obtained using a NN model  
415 trained only on near nadir view acquired products and used for classifying oblique view data are mostly conserved. However,  
416 the complexity brought in by the difference in the slant optical depth, which may translate to a noticeable difference in top-of-  
417 atmosphere signal levels, needs to be investigated in a full dedicated study.

418 Finally, the possibility to use S3/SLSTR products to train a neural network able to detect volcanic clouds in Sentinel-3/SLSTR  
419 granules might improve the overall accuracy of the classification.

420

#### 421 **Code availability**

422 The whole methodology is developed in MatLab environment. The source codes are available upon request to  
423 [ilaria.petracca@uniroma2.it](mailto:ilaria.petracca@uniroma2.it).

424

#### 425 **Data availability**

426 Terra-Aqua/MODIS data are distributed from the Level-1 and Atmosphere Archive & Distribution System (LAADS)  
427 Distributed Active Archive Center (DAAC) and they are available at: <https://ladsweb.modaps.eosdis.nasa.gov/search/>.

428 Sentinel-3/SLSTR data are distributed from the Copernicus Open Access Hub and they are available at:  
429 <https://scihub.copernicus.eu/dhus/#/home>.

430 The dataset used for this study are freely available on the Zenodo platform (<https://doi.org/10.5281/zenodo.7050771>).

431 **Author contributions**

432 IP and DDS developed algorithms, analyzed data and results and wrote the manuscript; MP developed algorithms and  
433 methodology, analyzed data and results and reviewed the manuscript; SC and LG analyzed data and results, provided reference  
434 data for validation task and wrote-reviewed the manuscript; FP supported the analysis of data and results, worked on the  
435 Himawari-8 analysis part of the manuscript, and reviewed the manuscript; LM and DS supported the analysis of data and  
436 results; FDF reviewed the manuscript, supervised the research and contributed to funding acquisition; GSaI supported the  
437 analysis of data and results and worked on validation; GSch supports the research and contributed to funding acquisition.  
438 All authors have read and agreed to the published version of the manuscript.

439 **Competing interests**

440 The authors declare that they have no conflict of interest.

441 **Disclaimer**

442 Publisher’s note: Copernicus Publications remains neutral with regard to jurisdictional claims in published maps and  
443 institutional affiliations.

444 **Special issue statement**

445 This article is part of the special issue “Satellite observations, in situ measurements and model simulations of the 2019 Raikoke  
446 eruption (ACP/AMT/GMD inter-journal SI)”. It is not associated with a conference.

447 **Acknowledgments**

448 The results shown in this work were obtained in the framework of the VISTA (Volcanic monItoring using SenTinel sensors  
449 by an integrated Approach) project, which was funded by ESA within the “EO Science for Society framework”  
450 [<https://eo4society.esa.int/projects/vista/>].

451 **Financial support**

452 Not applicable.

453 **References**

- 454 Atkinson, P. M., & Tatnall, A. R. L. (1997). Introduction Neural networks in remote sensing. *International Journal of Remote*  
455 *Sensing*, 18(4), 699–709. <https://doi.org/10.1080/014311697218700>
- 456 Bishop, C. M. (1994). Neural networks and their applications. *Review of Scientific Instruments*, 65(6), 1803–1832.  
457 <https://doi.org/10.1063/1.1144830>
- 458 Bourassa, A. E., Robock, A., Randel, W. J., Deshler, T., Rieger, L. A., Lloyd, N. D., Llewellyn, E. J. (Ted), & Degenstein, D.  
459 A. (2012). Large Volcanic Aerosol Load in the Stratosphere Linked to Asian Monsoon Transport. *Science*, 337(6090),  
460 78–81. <https://doi.org/10.1126/science.1219371>
- 461 Bruckert, J., Hoshyaripour, G. A., Horváth, Á., Muser, L. O., Prata, F. J., Hoose, C., & Vogel, B. (2022). Online treatment of  
462 eruption dynamics improves the volcanic ash and SO<sub>2</sub> dispersion forecast: Case of the 2019 Raikoke eruption.  
463 *Atmospheric Chemistry and Physics*, 22(5), 3535–3552. <https://doi.org/10.5194/acp-22-3535-2022>
- 464 Casadevall, T. J. (1994). The 1989–1990 eruption of Redoubt Volcano, Alaska: Impacts on aircraft operations. *Journal of*  
465 *Volcanology and Geothermal Research*, 62(1), 301–316. [https://doi.org/10.1016/0377-0273\(94\)90038-8](https://doi.org/10.1016/0377-0273(94)90038-8)Clarisse, L.,  
466 & Prata, F. (2016). Chapter 11—Infrared Sounding of Volcanic Ash. In S. Mackie, K. Cashman, H. Ricketts, A. Rust,  
467 & M. Watson (Eds.), *Volcanic Ash* (pp. 189–215). Elsevier. <https://doi.org/10.1016/B978-0-08-100405-0.00017-3>
- 468 Corradini, S., Merucci, L., & Prata, A. J. (2009). Retrieval of SO<sub>2</sub> from thermal infrared satellite measurements: Correction  
469 procedures for the effects of volcanic ash. *Atmospheric Measurement Techniques*, 2(1), 177–191.  
470 <https://doi.org/10.5194/amt-2-177-2009>
- 471 Corradini, S., Spinetti, C., Carboni, E., Tirelli, C., Buongiorno, M. F., Pugnaghi, S., & Gangale, G. (2008). Mt. Etna  
472 tropospheric ash retrieval and sensitivity analysis using Moderate Resolution Imaging Spectroradiometer  
473 measurements. *Journal of Applied Remote Sensing*, 2(1), 023550. <https://doi.org/10.1117/1.3046674>
- 474 Cox C., Polehampton E., & Smith D. (2021). *Sentinel-3 SLSTR Level-1 Algorithm and Theoretical Basis Document*, S3-TN-  
475 RAL-SL-032.
- 476 Craig, H., Wilson, T., Stewart, C., Outes, V., Villarosa, G., & Baxter, P. (2016). Impacts to agriculture and critical  
477 infrastructure in Argentina after ashfall from the 2011 eruption of the Cordón Caulle volcanic complex: An assessment  
478 of published damage and function thresholds. *Journal of Applied Volcanology*, 5(1), 7.  
479 <https://doi.org/10.1186/s13617-016-0046-1>

- 480 Delmelle, P., Stix, J., Baxter, P., Garcia-Alvarez, J., & Barquero, J. (2002). Atmospheric dispersion, environmental effects and  
481 potential health hazard associated with the low-altitude gas plume of Masaya volcano, Nicaragua. *Bulletin of*  
482 *Volcanology*, 64(6), 423–434. <https://doi.org/10.1007/s00445-002-0221-6>
- 483 Di Noia, A., & Hasekamp, O. P. (2018). Neural Networks and Support Vector Machines and Their Application to Aerosol and  
484 Cloud Remote Sensing: A Review. In A. Kokhanovsky (Ed.), *Springer Series in Light Scattering: Volume 1: Multiple*  
485 *Light Scattering, Radiative Transfer and Remote Sensing* (pp. 279–329). Springer International Publishing.  
486 [https://doi.org/10.1007/978-3-319-70796-9\\_4](https://doi.org/10.1007/978-3-319-70796-9_4)
- 487 Fawcett, T. (2006). An introduction to ROC analysis. *Pattern Recognition Letters*, 27(8), 861–874.  
488 <https://doi.org/10.1016/j.patrec.2005.10.010>
- 489 Francis, P. N., Cooke, M. C., & Saunders, R. W. (2012). Retrieval of physical properties of volcanic ash using Meteosat: A  
490 case study from the 2010 Eyjafjallajökull eruption. *Journal of Geophysical Research: Atmospheres*, 117(D20).  
491 <https://doi.org/10.1029/2011JD016788>
- 492 Gardner, M. W., & Dorling, S. R. (1998). Artificial neural networks (the multilayer perceptron)—A review of applications in  
493 the atmospheric sciences. *Atmospheric Environment*, 32(14), 2627–2636. [https://doi.org/10.1016/S1352-](https://doi.org/10.1016/S1352-2310(97)00447-0)  
494 [2310\(97\)00447-0](https://doi.org/10.1016/S1352-2310(97)00447-0)
- 495 Glaze, L. S., Baloga, S. M., & Wilson, L. (1997). Transport of atmospheric water vapor by volcanic eruption columns. *Journal*  
496 *of Geophysical Research: Atmospheres*, 102(D5), 6099–6108. <https://doi.org/10.1029/96JD03125>
- 497 Gorkavyi, N., Krotkov, N., Li, C., Lait, L., Colarco, P., Carn, S., DeLand, M., Newman, P., Schoeberl, M., Taha, G., Torres,  
498 O., Vasilkov, A., & Joiner, J. (2021). Tracking aerosols and SO<sub>2</sub> clouds from the Raikoke eruption: 3D view from  
499 satellite observations. *Atmospheric Measurement Techniques*, 14(12), 7545–7563. [https://doi.org/10.5194/amt-14-](https://doi.org/10.5194/amt-14-7545-2021)  
500 [7545-2021](https://doi.org/10.5194/amt-14-7545-2021)
- 501 Gray, T. M., & Bennartz, R. (2015). Automatic volcanic ash detection from MODIS observations using a back-propagation  
502 neural network. *Atmospheric Measurement Techniques*, 8(12), 5089–5097. <https://doi.org/10.5194/amt-8-5089-2015>
- 503 Haywood, J., & Boucher, O. (2000). Estimates of the direct and indirect radiative forcing due to tropospheric aerosols: A  
504 review. *Reviews of Geophysics*, 38(4), 513–543. <https://doi.org/10.1029/1999RG000078>

505 Horwell, C. J., & Baxter, P. J. (2006). The respiratory health hazards of volcanic ash: A review for volcanic risk mitigation.  
506 *Bulletin of Volcanology*, 69(1), 1–24. <https://doi.org/10.1007/s00445-006-0052-y>

507 Horwell, C. J., Baxter, P. J., Hillman, S. E., Calkins, J. A., Damby, D. E., Delmelle, P., Donaldson, K., Dunster, C., Fubini,  
508 B., Kelly, F. J., Le Blond, J. S., Livi, K. J. T., Murphy, F., Natrass, C., Sweeney, S., Tetley, T. D., Thordarson, T.,  
509 & Tomatis, M. (2013). Physicochemical and toxicological profiling of ash from the 2010 and 2011 eruptions of  
510 Eyjafjallajökull and Grímsvötn volcanoes, Iceland using a rapid respiratory hazard assessment protocol.  
511 *Environmental Research*, 127, 63–73. <https://doi.org/10.1016/j.envres.2013.08.011>

512 Mather, T. A., Pyle, D. M., & Oppenheimer, C. (2003). Tropospheric volcanic aerosol. In A. Robock & C. Oppenheimer  
513 (Eds.), *Geophysical Monograph Series* (Vol. 139, pp. 189–212). American Geophysical Union.  
514 <https://doi.org/10.1029/139GM12>

515 McKee, K., Smith, C. M., Reath, K., Snee, E., Maher, S., Matoza, R. S., Carn, S., Mastin, L., Anderson, K., Damby, D.,  
516 Roman, D. C., Degterev, A., Rybin, A., Chibisova, M., Assink, J. D., de Negri Leiva, R., & Perttu, A. (2021).  
517 Evaluating the state-of-the-art in remote volcanic eruption characterization Part I: Raikoke volcano, Kuril Islands.  
518 *Journal of Volcanology and Geothermal Research*, 419, 107354. <https://doi.org/10.1016/j.jvolgeores.2021.107354>

519 Menzel, W. P., Frey, R. A., & Baum, B. A. (2015). Cloud top properties and cloud phase algorithm theoretical basis document.  
520 73.

521 Millán, L., Santee, M. L., Lambert, A., Livesey, N. J., Werner, F., Schwartz, M. J., Pumphrey, H. C., Manney, G. L., Wang,  
522 Y., Su, H., Wu, L., Read, W. G., & Froidevaux, L. (2022). The Hunga Tonga-Hunga Ha’apai Hydration of the  
523 Stratosphere. *Geophysical Research Letters*, 49(13), e2022GL099381. <https://doi.org/10.1029/2022GL099381>

524 Murcray, D. G., Murcray, F. J., Barker, D. B., & Mastenbrook, H. J. (1981). Changes in Stratospheric Water Vapor Associated  
525 with the Mount St. Helens Eruption. *Science*, 211(4484), 823–824. <https://doi.org/10.1126/science.211.4484.823>

526 Muser, L. O., Hoshyaripour, G. A., Bruckert, J., Horváth, Á., Malinina, E., Wallis, S., Prata, F. J., Rozanov, A., von Savigny,  
527 C., Vogel, H., & Vogel, B. (2020). Particle aging and aerosol–radiation interaction affect volcanic plume dispersion:  
528 Evidence from the Raikoke 2019 eruption. *Atmospheric Chemistry and Physics*, 20(23), 15015–15036.  
529 <https://doi.org/10.5194/acp-20-15015-2020>



- 530 Nishihama M., Blanchette J., Fleig A., Freeze M., Patt F. & Wolfe R. (1998). *MODIS Level 1A Earth Location: Algorithm*  
531 *Theoretical Basis Document Version 3.0.*
- 532 Oppenheimer, C., Scaillet, B., & Martin, R. S. (2011). Sulfur Degassing From Volcanoes: Source Conditions, Surveillance,  
533 Plume Chemistry and Earth System Impacts. *Reviews in Mineralogy and Geochemistry*, 73(1), 363–421.  
534 <https://doi.org/10.2138/rmg.2011.73.13>
- 535 Pavolonis, M. J. (2010). Advances in Extracting Cloud Composition Information from Spaceborne Infrared Radiances—A  
536 Robust Alternative to Brightness Temperatures. Part I: Theory. *Journal of Applied Meteorology and Climatology*,  
537 49(9), 1992–2012. <https://doi.org/10.1175/2010JAMC2433.1>
- 538 Pavolonis, M., & Sieglaff, J. (2012). *GOES-R Advanced Baseline Imager (ABI) Algorithm Theoretical Basis Document For*  
539 *Volcanic Ash (Detection and Height)*. 71.
- 540 Picchiani, M., Chini, M., Corradini, S., Merucci, L., Piscini, A., & Frate, F. D. (2014). Neural network multispectral satellite  
541 images classification of volcanic ash plumes in a cloudy scenario. *Annals of Geophysics*, 57.  
542 <https://doi.org/10.4401/ag-6638>
- 543 Picchiani, M., Chini, M., Corradini, S., Merucci, L., Sellitto, P., Del Frate, F., & Stramondo, S. (2011). Volcanic ash detection  
544 and retrievals using MODIS data by means of neural networks. *Atmospheric Measurement Techniques*, 4(12), 2619–  
545 2631. <https://doi.org/10.5194/amt-4-2619-2011>
- 546 Picchiani, M., Del Frate, F., & Sist, M. (2018). A Neural Network Sea-Ice Cloud Classification Algorithm for Copernicus  
547 Sentinel-3 Sea and Land Surface Temperature Radiometer. *IGARSS 2018 - 2018 IEEE International Geoscience and*  
548 *Remote Sensing Symposium*, 3015–3018. <https://doi.org/10.1109/IGARSS.2018.8517857>
- 549 Piscini, A., Carboni, E., Del Frate, F., & Grainger, R. G. (2014). Simultaneous retrieval of volcanic sulphur dioxide and plume  
550 height from hyperspectral data using artificial neural networks. *Geophysical Journal International*, 198(2), 697–709.  
551 <https://doi.org/10.1093/gji/ggu152>
- 552 Polehampton E., Cox C., Smith D., Ghent D., Wooster M., Xu W., Bruniquel J. & Dransfeld S. (2021). *Copernicus Sentinel-*  
553 *3 SLSTR Land User Handbook*, 3MPC.ACR.HBK.002.
- 554 Prata, A. J. (1989a). Infrared radiative transfer calculations for volcanic ash clouds. *Geophysical Research Letters*, 16(11),  
555 1293–1296. <https://doi.org/10.1029/GL016i011p01293>

- 556 Prata, A. J. (1989b). Observations of volcanic ash clouds in the 10-12  $\mu\text{m}$  window using AVHRR/2 data. *International Journal*  
557 *of Remote Sensing*, 10(4–5), 751–761. <https://doi.org/10.1080/01431168908903916>
- 558 Prata, A. J., & Grant, I. F. (2001). *Determination of mass loadings and plume heights of volcanic ash clouds from satellite*  
559 *data*. <https://publications.csiro.au/rpr/pub?list=BRO&pid=procite:d76866c5-98ff-40a4-a7cb-80c5fad7f6da>
- 560 Prata, A. T., Grainger, R. G., Taylor, I. A., Povey, A. C., Proud, S. R., & Poulsen, C. A. (2022). Uncertainty-bounded estimates  
561 of ash cloud properties using the ORAC algorithm: Application to the 2019 Raikoke eruption. *Atmospheric*  
562 *Measurement Techniques Discussions*, 1–35. <https://doi.org/10.5194/amt-2022-166>
- 563 Prata, F., Bluth, G., Rose, B., Schneider, D., & Tupper, A. (2001). Comments on “Failures in detecting volcanic ash from a  
564 satellite-based technique.” *Remote Sensing of Environment*, 78(3), 341–346. [https://doi.org/10.1016/S0034-](https://doi.org/10.1016/S0034-4257(01)00231-0)  
565 [4257\(01\)00231-0](https://doi.org/10.1016/S0034-4257(01)00231-0)
- 566 Rose, W. I., Delene, D. J., Schneider, D. J., Bluth, G. J. S., Krueger, A. J., Sprod, I., McKee, C., Davies, H. L., & Ernst, G. G.  
567 J. (1995). Ice in the 1994 Rabaul eruption cloud: Implications for volcano hazard and atmospheric effects. *Nature*,  
568 375(6531), 477–479. <https://doi.org/10.1038/375477a0>
- 569 Shinohara, H. (2008). Excess degassing from volcanoes and its role on eruptive and intrusive activity. *Reviews of Geophysics*,  
570 46(4). <https://doi.org/10.1029/2007RG000244>
- 571 Solomon, S., Daniel, J. S., Neely, R. R., Vernier, J.-P., Dutton, E. G., & Thomason, L. W. (2011). The Persistently Variable  
572 “Background” Stratospheric Aerosol Layer and Global Climate Change. *Science*, 333(6044), 866–870.  
573 <https://doi.org/10.1126/science.1206027>
- 574 Toller G. N., Isaacman, A., Kuyper J., Geng X. & Xiong J. (2017). *MODIS Level 1B Product User’s Guide*. 62.
- 575 Vermote, E. F. & Vermeulen A. (1999). *MODIS Algorithm Technical Background Document, ATMOSPHERIC*  
576 *CORRECTION ALGORITHM: SPECTRAL REFLECTANCES (MOD09)*.
- 577 Vogl, T. P., Mangis, J. K., Rigler, A. K., Zink, W. T., & Alkon, D. L. (1988). Accelerating the convergence of the back-  
578 propagation method. *Biological Cybernetics*, 59(4), 257–263. <https://doi.org/10.1007/BF00332914>
- 579 Xu, J., Li, D., Bai, Z., Tao, M., & Bian, J. (2022). Large Amounts of Water Vapor Were Injected into the Stratosphere by the  
580 Hunga Tonga–Hunga Ha’apai Volcano Eruption. *Atmosphere*, 13(6), 912. <https://doi.org/10.3390/atmos13060912>
- 581